

Anisotropic spreading of liquid metal on a rough intermetallic surface

Wen Liu* Dušan P. Sekulić†

Abstract

An anisotropic wicking of molten Sn-Pb solder over an intermetallic rough surface has been studied. The phenomenon features preferential spreading and forming of an elliptical spread domain. A theoretically formulated model was established to predict the ratio of the wicking distance along the long axis (r_x) to that along the short axis (r_y) of the final wicking pattern. The phenomenon was simultaneously experimentally observed and recorded with a hotstage microscopy technique. The anisotropic wicking is established to be caused by a non-uniform topography of surface micro structures as opposed to an isotropic wicking on an intermetallic surface with uniformly distributed surface micro features. The relative deviation between the theoretically predicted r_x/r_y ratio and the corresponding average experimental value is 5%. Hence, the small margin of error confirms the validity of the proposed theoretical model of anisotropic wicking.

Keywords: Surface tension driven flow, anisotropic spreading, rough surface.

1 Introduction

Wetting of the topographically complex interfaces and associated wicking phenomena over rough surfaces or porous domains have been for a long time of keen interest in a broad range of applications, including brazing, soldering, inkjet printing and micro fluid management [1-3]. A number of research

*Department of Mechanical Engineering, College of Engineering, University of Kentucky, Lexington, KY 40506, USA

†Department of Mechanical Engineering, College of Engineering, University of Kentucky, Lexington, KY 40506, USA, e-mail: sekulicd@engr.uky.edu

efforts have been made on isotropic wetting/wicking on rough/structured surfaces in the last two decades [4-13]. Virtually all of these studies describe only the isotropic wetting/wicking phenomena. In most cases, a classical Washburn type flow model [14] was implemented. In recent years, an anisotropic wetting/wicking begins to gain more attention as developments in surface engineering and other micro scale applications became more prominent. Anisotropic wetting/wicking is usually achieved at a room temperature by using (i) micro/nano scale regular grooved structures engineered on a surface [15-17], (ii) micro/nano symmetric/asymmetric structures [18-20], and (iii) selective chemical patterning on surfaces [21-22]. As a rule, these studies are not fully devoted to kinetics of spreading. Only a few theoretical models describing the liquid flow kinetics were reported under these conditions.

In this study, we demonstrate first an anisotropic wicking phenomenon at a temperature of ~ 260 °C for the case of spreading of a molten Sn-Pb solder. This liquid metal spreading is caused by the capillary action involving micro scale topographic features on the so called IMC3 surface [10, 11]. Subsequently, the focus is shifted toward establishing a theoretical model for predicting the ratio of the wicking distances along two orthogonal and directions. Finally, corroboration of the theoretical model and empirical data was performed.

2 Phenomenological description and problem formulation

A scanning electron microscopy (SEM) image as well as a real time in situ image generated with the hot-stage optical microscopy presented in Figures 1 (a) and (b) show the topography of IMC1 surface and associated wicking of molten Sn-Pb solder over that surface. It is easy to notice that IMC1 surface has uniformly distributed topographical features – micro scallop-shaped grains. Such uniformity leads to a uniform, circular pattern of wicking of the molten metal, see Fig. 1 (b). A successful analytical model for such wicking was reported recently in [12]. Figures 1 (c) and (d) illustrate the topography of a modified surface, IMC3, for which the associated wicking of the same liquid metal as for IMC1 appears to be dramatically different. One should notice a marked difference in topography between IMC1 and IMC3. Instead of having uniform distributed grains like IMC1, IMC3 has grown grains which are distributed non-uniformly; with a stark anisotropy

in the two orthogonal directions. Such non-uniformity of the topographical features leads to an anisotropic wicking of the molten metal. Figure 1 (d) offers an ultimate wicking pattern of the molten Sn-Pb solder on an IMC3 surface. This pattern resembles an ellipse, featuring a long and a short axis.

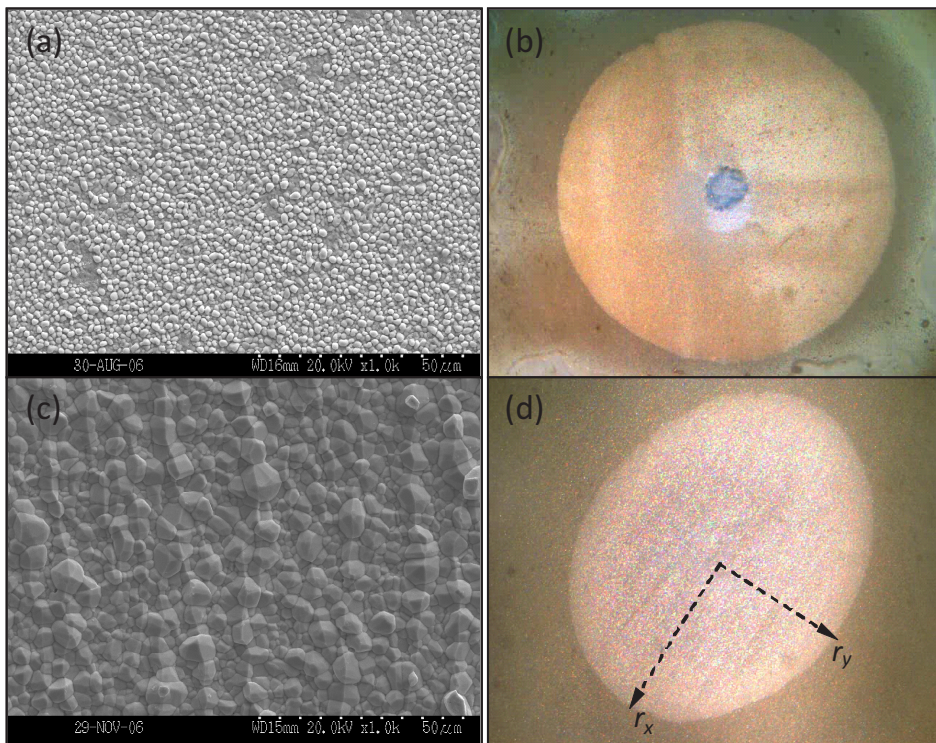


Figure 1: (a) SEM images Topography of IMC1 surface. (b) Wicking pattern (Circle) of Sn-Pb on IMC1. (c) Topography of IMC3 surface. (d) Wicking pattern (Ellipse) of Sn-Pb on IMC3.

A phenomenological description of the spreading (wicking) is as follows. After a pellet of a solid Sn-Pb solder (~ 0.2 mm equivalent radius and ~ 0.05 mm thickness), was placed on the pre-prepared IMC1/IMC3 surface and exposed to melting, liquid metal was sucked into the surface roughness topographical features composed of a network of open triangular (in the first approximation) grooves. For IMC1, Figure 1(a) and (b), the uniform distribution of grains and associated network of grooves leads to an isotropic wicking that results in a final wicking pattern of an almost perfect circle. For

IMC3, Figure 1 (c) and (d), the network channels formed by grains featuring non-uniform distribution directs molten metal into different directions with a different wicking rate. The most pronounced difference occurs in two orthogonal directions and results in an appearance of a long and short axis of the final wicking pattern with an elliptical shape. Figures 1 (b) and (d) indicate clearly ultimate triple line locations of molten metal on IMC1 and IMC3 surfaces, respectively.

3 Theoretical model

In Figure 2, a model configuration is presented for two orthogonal directions. The x and y axes represent the directions of the long and short radii of the preferential directions of an ellipse of Figure 1 (d). For both directions, a control volume within a very small angle δ is taken for analysis. The radius r_0 is the initial radius of the solder material; r_x represents a random radial location of the wicking front radius within the range from r_0 to the final radius, associated with $u_x(r_x)$ and t ; r_y represents the same for the y direction. The model is established with the assumptions discussed in [12] as the experimental setup and materials used in these two series of experiments are identical.

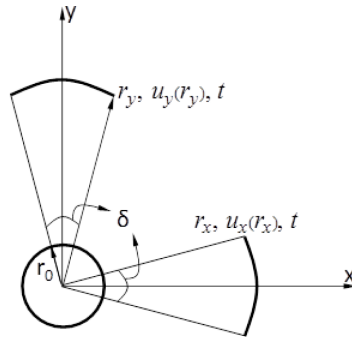


Figure 2: Model configuration for an anisotropic wicking on IMC3 surface

The velocity field must be consistent with the continuity equation and the Darcy's Law implemented for an arbitrary liquid metal differential ele-

ment within the marked control volume, [23]

$$\mathbf{v} = -\frac{1}{\mu}[\mathbf{K} \cdot \nabla p] \quad (1)$$

where \mathbf{v} is the velocity vector, μ is the dynamic viscosity, and \mathbf{K} is an intrinsic permeability tensor of the porous medium. The pressure gradient ∇p is associated with the real flow path driven by the capillary force. The simplified equation for the velocity associated with r_x in x direction may be expressed as

$$u_x(r_x) = \frac{k_x}{\mu} \left(-\frac{\partial p}{\partial x} \right) \quad (2)$$

The velocity of liquid while it flows through the location of r_x at the corresponding time instant t can also be expressed by definition as

$$u_x(r_x) = \frac{d(r_x \tau_x)}{dt} \quad (3)$$

where τ_x is tortuosity along the long axis, defined as the ratio of the real extended curved path that fluid passes through the micro channels to the shortest distance between the ends of the real path.

Equality of velocity $u_x(r_x)$ expressions of in equation (2) by Darcy's law and definition of velocity in equation (3) will lead:

$$\frac{k_x}{\mu} \left(-\frac{\partial p}{\partial x} \right) = \frac{d(r_x \tau_x)}{dt} \quad (4)$$

The product $(\tau_x r_x)$, which corresponds to an arbitrary position r_x , is the path of the molten metal flowing through IMC3 surface alterations. This product introduces tortuosity into the model, τ_x [24]. The tortuosity τ_x is along the long axis direction on the IMC3 surface.

The pressure gradient at a location r_x in equation (2) can be approximated as

$$-\frac{\partial p}{\partial x} \Big|_{r_x} \sim \frac{\Delta p}{\tau_x r_x} \quad (5)$$

Combining Eq.(4) and (5) leads to

$$\frac{k_x}{\mu \tau_x^2} \Delta p = r_x \frac{dr_x}{dt} \quad (6)$$

The pressure gradient established along the porous domain in equation (2) is caused by a capillary force exerted on the molten metal flowing through

the open grooves formed by roughness features of the surface. In order to assess the capillary pressure, capillary force F_σ and associated area $A(\alpha, \theta)$ are introduced. The dominant feature of surface grooves is experimentally assessed to be of a V-shape [25]. Based on [12], [26], but with the groove of the profile height h_0 only partially filled ($h = \eta h_0$), one gets

$$F_\sigma = \frac{2\eta h_0 \sigma}{\sin \alpha} \left[\cos \theta - \frac{(\alpha - \theta) \cos \alpha}{\sin(\alpha - \theta)} \right] \quad (7)$$

where η is the filling factor which is introduced in our recent work [12], [13].

The actual cross sectional area of liquid in a single V-groove can be expressed as, [13]

$$A(\alpha, \theta) = (\eta h_0)^2 \frac{\sin^2(\alpha - \theta) \tan \alpha - (\alpha - \theta) + \sin(\alpha - \theta) \cos(\alpha - \theta)}{\tan^2(\alpha) \sin^2(\alpha - \theta)} \quad (8)$$

Note that equation (10) includes an impact of the filling factor η [12, 13], not present in the modeling referred to in [26].

With $\Delta p = F_\sigma/A(\alpha, \theta)$, F_σ and $A(\alpha, \theta)$ from equation (7) and (8) respectively, an integration of equation (6) with respect to time from t_0 to t across the domain of spreading from r_0 to r_x , respectively, leads to

$$r_x^2 = 4 \frac{1}{\eta h_0} \frac{k_x \sigma}{\tau_x^2 \mu} G(\alpha, \theta) t + r_0^2 \quad (9)$$

Applying the same consideration for the flow in the y direction will lead to the relation between r_y and t , that is

$$r_y^2 = 4 \frac{1}{\eta h_0} \frac{k_y \sigma}{\tau_y^2 \mu} G(\alpha, \theta) t + r_0^2 \quad (10)$$

Equations (9) and (10) include both the same geometric parameter, G , i.e.,

$$G(\alpha, \theta) = \frac{\left[\cos \theta - \frac{(\alpha - \theta) \cos \alpha}{\sin(\alpha - \theta)} \right] \tan^2(\alpha) \sin^2(\alpha - \theta)}{\sin \alpha [\sin^2(\alpha - \theta) \tan \alpha - (\alpha - \theta) + \sin(\alpha - \theta) \cos(\alpha - \theta)]} \quad (11)$$

In Eq.(11), $G(\alpha, \theta)$ is a non-dimensional geometrical parameter stemming from the topography of a micro groove. Equations (9), (10) and (11) offer a correlation between an instantaneous location of the triple line, r_x , r_y and the spreading time, t . They also show that the spreading rate is related to the topography of the surface and the liquid properties. The ratio

of the two radii, Equations (9) and (10), offers the relationship between the wicking distance in x direction (the long axis) to that in the y direction (the short axis).

$$\frac{r_x}{r_y} = \left(\frac{\frac{k_x}{\tau_x^2} + \frac{\mu\eta h_0 r_0^2}{4\sigma G(\alpha, \theta)t}}{\frac{k_y}{\tau_y^2} + \frac{\mu\eta h_0 r_0^2}{4\sigma G(\alpha, \theta)t}} \right)^{1/2} \approx \frac{\tau_y}{\tau_x} \left(\frac{k_x}{k_y} \right)^{1/2} \quad (12)$$

where τ_x , τ_y are the tortuosity along the long axis (x-axis) and the short axis (y-axis) of the ellipse, respectively. The quantities k_x and k_y are the permeabilities associated with the x-axis and y axis, respectively. Hence, the ratio of the wicking radii in two orthogonal directions is expressed as a function of tortuosity and permeability. A careful consideration of the order of magnitude of the terms on the right-hand side of the first equality in equation (12) reveals that $[\mu\eta h_0 r_0^2 / 4\sigma G(\alpha, \theta)t] \ll [k_x / \tau_x^2]$, where $[\mu\eta h_0 r_0^2 / 4\sigma G(\alpha, \theta)t] \sim O(10^{-17})$ and $[k_x / \tau_x^2] \sim [k_y / \tau_y^2] \sim O(10^{-14})$. Consequently, the second equality would hold with a high level of precision.

4 Materials and experimental procedures

The substrate was manufactured from a virgin Cu sheet. A Cu plate was dipped into the molten Sn at 260 °C, then the re-solidified Sn coating was etched away to expose the IMC layer formed at the interface. The details of this procedure were described in [10, 11].

Subsequently, the manufactured substrate was exposed to an experimental procedure aimed at establishing the kinetics of the liquid metal spreading. The hot stage microscopy was used to analyze kinetics of the triple line movement. A substrate coupon having overall dimensions of 10 mm × 10 mm × 0.3 mm (or 0.5 mm) is positioned within the chamber of the LINKAM THMS 600 hot stage installed on an OLIMPUS BX51M optical microscope. A solder specimen was covered with a thin layer of RMA flux [EC-19S-8, Tamura Corp.]. The chamber was filled with ultra high purity N₂ (99.999%), after purging with nitrogen for 120 minutes before an initiation of the heating cycle. The purging has secured at least 30 chamber's volume replacements. The purging was continued during a test. The heating cycle consists of a ramp up, dwell and quench assisted by a liquid nitrogen cooling system.

The heating ramp-up was 100°C/min and the cooling ramp-down was 80°C/min. Temperature stability was at the level of 0.1 K. Verification of the actual solder temperature was performed by comparing temperature

readings for a given instant of time at the onset of melting, with the eutectic solder melting point temperature known. Correspondingly, temperature readings were corrected and the bias was eliminated. The series of thermal contact resistances includes (i) Ag heating block - quartz glass interface, (ii) quartz - glass -interface - substrate, and (iii) substrate-solder interface, in presence of flux. The peak temperature is set to be consistently 30K above the liquidus temperature of the corresponding solder. During the heating/cooling cycle, digital imaging is performed with a 22 frames/s digital camera system. Movie clips were digitally decomposed into individual frames and associated with digitally recorded corresponding substrate temperature histories. The ratio of the wicking distance along the long axis to that along the short axes r_x/r_y indicated in Figure 1 (d) is experimentally measured after performing four different tests. Data handling was performed using the ImagePro Plus software. The measured ratios were 1.25, 1.40, 1.26 and 1.47, respectively. The average value is 1.35 with the standard deviation of 0.11.

Each IMC surface was also scanned by a Zygo 3D optical surface profiler for an area of 1.447 mm \times 1.085 mm with an optical magnification of 200 \times . The Zygo optical profilometer has a vertical resolution of 0.1 nm and field of view of 0.04 – 17.5 mm. The surface topography measurements were done at ambient conditions.

Figure 3 (a) and (b) offers respectively the topography analysis results for IMC1 and IMC3 generated by the Zygo 3D optical surface profiler. The surface scanning was conducted on a random location with a scanning area of 1.447mm \times 1.085mm on both IMC1 and IMC3 surfaces. The scanning results indicate clearly the topographic difference of IMC1 and IMC3 surfaces. Comparing to IMC1, the surface topographical structures on IMC3 are with a larger size, and are distributed with a much less uniformity and a preferential anisotropy. The surface structures on IMC1 and IMC3, with various sizes and different distributions of the surface topographical features, resulted in either isotropic or anisotropic wicking behavior, respectively.

5 Results and discussion

The permeability is expressed as a function of the surface porosity [27], [12] and roughness [28].

$$k_{theor} = \frac{\varepsilon}{6} \left(\frac{2\varepsilon}{B} \right)^2 \quad (13)$$

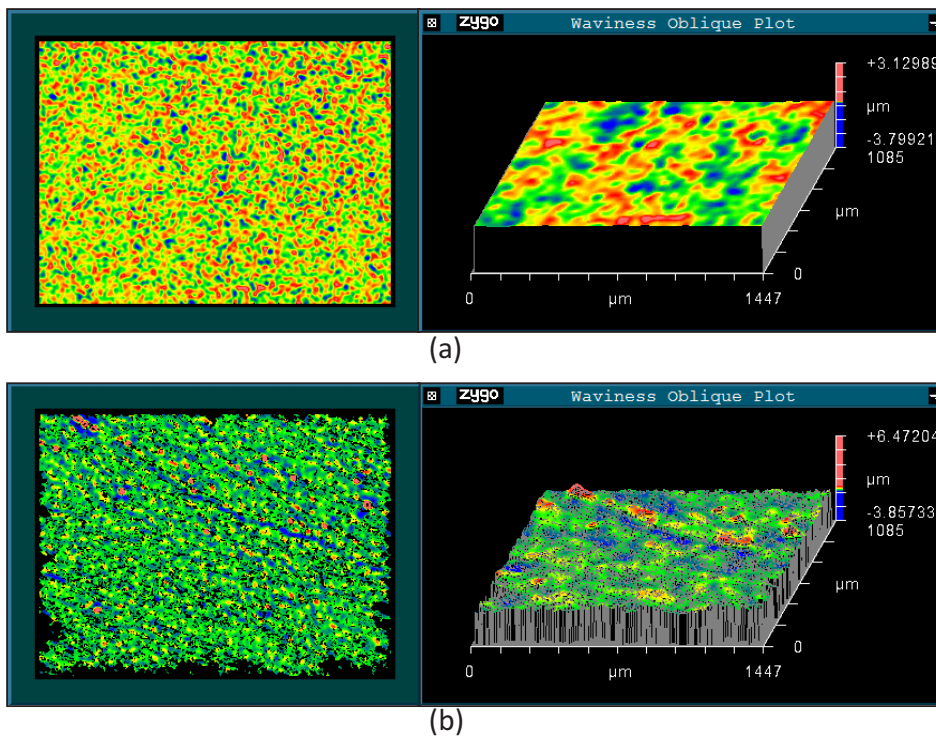


Figure 3: (a) Roughness analysis of IMC1 surface with Zygo optical profiler. (b) Roughness analysis of IMC3 surface with Zygo optical profiler.

where k_{theor} is theoretically derived permeability; ε is the porosity; B is the ratio of total surface area of voids throughout the porous medium to the total volume of the porous medium. Note that the total volume of the porous medium in this study is the product of the projected area and the height of the IMC substrate.

Tortuosity and surface porosity have a correlation expressed as $\tau = \varepsilon^{-1.2}$, [24], [29]. The surface porosity of IMC3 is measured at four different random locations, based on atomic force microscope (AFM) scanning results. It is found it to be 0.65 for x direction and 0.59 for y direction, with standard deviations of 0.04 and 0.06 respectively. The ratio of the surface roughness associated with the y direction to that associated with the x direction is measured to be 1.1, with the standard deviation of 0.1. The ratio of the final wicking radius along x-axis to the radius along the y-axis is experimentally measured for four different wicking tests on IMC3 surface and the average

value of that ratio is 1.35, with the standard deviation of 0.11. With all the measured parameters for the topographical features, the theoretical ratio presented in equation (12) is calculated to be 1.42. Correspondingly, the relative deviation between theoretically predicted r_x/r_y ratio (1.42) and the average experimental value (1.35) is only 5%. This small margin of error verifies the validity of the theoretically derived model of the considered anisotropic wicking.

6 Conclusion

An anisotropic wicking phenomenon involving spreading of molten Sn-Pb solder on a fabricated intermetallic rough surface was modeled and studied experimentally with the aid of hotstage microscopy *in situ* and in real time. Comparison of IMC1 and IMC3 indicates that IMC3 has non-uniformly distributed surface structures. The rough intermetallic surface is ultimately characterized by experimentally measured surface porosity and roughness. A theoretically derived model was established to predict the ratio of wicking distance along the long axis (r_x) to that along the short axis (r_y) of the final wicking pattern featuring an elliptical shape. The relative deviation between theoretically predicted r_x/r_y ratio and the average experimental value is around 5%. This small margin of error proves validity of the theoretically established model. Thus, an anisotropic wicking can be predicted with an analytical model proposed.

Acknowledgment

This research is supported in part through KSEF-829-RDE-007 and KSEF-1490-RDE-010 grants. Authors appreciated preliminary experimental work conducted by and assistance of Dr. H. Zhao and Dr. H. Wang during their tenure as postdoctoral fellow and a graduate student, respectively in the Brazing Laboratory of the University of Kentucky.

References

- [1] De Gennes, P.G. (1985) Wetting: statics and dynamics, *Reviews of Modern Physics*, Vol. 57, No. 3, pp.827-863
- [2] Bonn, D.; Egger, J.; Indekeu, J.; Meunier, J. and Rolley, E. (2009) Wetting and spreading, *Reviews of Modern Physics*, Vol. 81, pp.739-805

- [3] Quéré, D. (2008) Wetting and Roughness, *Ann. Rev. Mater. Res.*, Vol. 38, pp.71-99
- [4] Sekulic, D. P. (2011) Wetting and spreading of liquid metal through open micro grooves and surface alterations, *Heat Transfer Engineering*, Vol. 32 (7-8), pp. 648-657
- [5] Cazabat, A.M.; Cohen Stuart, M.A. (1986) Dynamics of wetting: Effects of surface roughness, *J. Phys. Chem.*, Vol.90, pp.5845-5849
- [6] Bico, J.; Tordeux, C.; Quéré, D. (2001) Rough wetting, *Europhys. Lett.*, Vol. 55 (2), pp.214-220
- [7] Dussaud, A.D.; Adler, P.M.; Lips, A. (2003) Liquid transport in the networked microchannels of the skin surface, *Langmuir*, Vol. 19, pp.7341-7345
- [8] Hay, K.M.; Dragila, M.I.; Liburdy, J. (2008) Theoretical model for the wetting of a rough surface, *Journal of Colloid and Interface Science*, Vol. 325, pp.472-477
- [9] Chen, Y.K.; Melvin, L.S.; Rodriguez, S.; Bell, D.; Weislogel, M.M. (2009) Capillary driven flow in micro scale surface structures, *Microelectronic Engineering*, Vol. 86, pp.1317-1320
- [10] Zhao, H.; Wang. H.; Sekulic, D.P.; Qian, Y. (2009a) Spreading Kinetics of Liquid Solders over an intermetallic solid surface, Part 1: Lead solders, *Journal of Electronic Materials*, Vol.38, pp.1838-1845
- [11] Zhao, H.; Wang. H.; Sekulic, D.P.; Qian, Y. (2009b) Spreading Kinetics of Liquid Solders over an intermetallic solid surface, Part 2: Lead-free solders, *Journal of Electronic Materials*, Vol.38, pp.1846-1854
- [12] Liu, W and Sekulic, D.P (2011) Capillary driven molten metal flow over topographically complex substrates, *Langmuir*, Vol. 27(11), pp. 6720-6730
- [13] Liu, W.; Li, Y.; Cai, Y.; Sekulic, D.P. (2011) Capillary Rise of Liquids over a Microstructured Solid Surface, *Langmuir*, Vol. 27(23), pp. 14260-14266
- [14] Washburn, E.W. (1921) The dynamics of capillary flow, *Phys. Rev.* Vol. 17, pp. 273-283.
- [15] Zhao, Y., Lu, Q., Li, M., and Li, X. (2007) Anisotropic wetting characteristics on submicrometer-scale periodic grooved surface, *Langmuir*, Vol. 23, pp. 6212-6217
- [16] Li, W., Fang, G., Li, Y., and Quan, G. (2008) Anisotropic wetting behavior arising from super hydrophobic surfaces: parallel grooved structure, *J. Phys. Chem. B*, Vol.112, pp. 7234-7243
- [17] Xia, D. and Brueck, S.R.J. (2008) Strongly anisotropic wetting on one-dimensional nanopatterned surfaces, *Nano Letters*, Vol.8, No.9, pp. 2819-2824

- [18] Priest, C., Albrecht, T.W.J., Sedev, R. and Ralston, J. (2009) Asymmetric wetting hysteresis on hydrophobic microstructured surfaces, *Langmuir*, Vol. 25(10), pp. 5655-5660
- [19] Anantharaju, N., Panchagnula, V., and Vedantam, S. (2009) Asymmetric wetting of patterned surfaces composed of intrinsically hysteretic materials, *Langmuir*, Vol. 25(13), pp. 7410-7415
- [20] Chu, K-H., Xiao, R. and Wang, E.N. (2010) Uni-directional liquid spreading on asymmetric nanostructured surfaces, *Nature Materials*, Vol. 9, pp. 413-417
- [21] Dupuis, A, Leopoldes, J., Bucknall, D. G. & Yeomans, J. M (2005) Control of drop positioning using chemical patterning, *Appl. Phys. Lett.*, Vol. 87, 024103
- [22] Gleiche, M., Chi, L. F. & Fuchs, H. Nanoscopic channel lattices with controlled anisotropic wetting, *Nature*, Vol. 403, pp. 173-175
- [23] *Flow through Porous Media* (1970) American Chemical Society (Symposium on Flow Through Porous Media, 1969, Washington, D.C.)
- [24] Epstein, N. (1989) On Tortuosity and the Tortuosity Factor in Flow and Diffusion through Porous Media, *Chemical Engineering Science*, Vol. 44, No. 3, pp.777-779
- [25] Liu, W., Lu, L., Li, Y., Cai, Y. and Sekulic, D.P. (2011) Preferential spreading of molten metal over an anisotropically microstructured surface, to be published.
- [26] Rye, R.R.; Mann, J.A. Jr.; Yost, F.G. (1996) The flow of liquid in surface grooves, *Langmuir*, Vol.12, pp.555-565
- [27] Hubbert, M.K. (1957) Darcy's Law and the Field Equations of the Flow of Underground Fluids, *Hydrological Sciences Journal*, Vol.2, Issue 1 (March 1957), pp.23-59
- [28] Wenzel, R.N. (1936) Resistance of Solid Surfaces to Wetting by Water, *Industrial and Engineering Chemistry*, Vol. 28, No. 8, pp. 988-994
- [29] Boving, T.B., and Grathwohl, P. (2001) Tracer Diffusion Coefficients in Sedimentary Rocks: Correlation to Porosity and Hydraulic Conductivity, *Journal of Contaminant Hydrology*, Vol.53, pp.85-100

Submitted in June 2011

Anizotropno prostiranje tečnog metala na hrapavoj metalnoj površini

Anizotropno prostiranje rastopljene legure Sn-Pb koje je uzrokovano dejstvom sila površinskog napona preko hrapavog metalnog substrata analizirano je korišćenjem teorijskog modela i serije eksperimenata. Anizotropna topografija substrata uzrokuje anizotropno prostiranje trojne linije tečnosti i formiranje eliptičnog prostornog domena. Analitički model je zasnovan na uvažavanju zakona Darci-ja i očuvanja mase. Analizirana pojava je eksperimentalno registrovana u realnom vremenu, *in situ*, korišćenjem optičke mikroskopije na povišenim temperaturama. Topografija substrata je analizirana optičkom profilometrijom i atomskom mikroskopijom. Relativno odstupanje količnika glavnih radijusa eliptičnog domena prostiranja određeno teorijskim predviđanjem i eksperimentalnim merenjem je reda veličine 5 procenata.